Hindawi
Advances in Civil Engineering
Volume 2018, Article ID 8362319, 18 pages
https://doi.org/10.1155/2018/8362319

Research Article

Steel Plate Cold-Rolled Section Steel Embedded High-Strength Concrete Low-Rise Shear Wall Seismic Performance

Min Gan,[1,2] Yu Yu,[1,2] Liren Li,[1,2] and Xisheng Lu[1,2]

[1]*School of Civil Engineering, Chongqing University, Chongqing 400045, China*
[2]*Key Laboratory of New Technology for Construction of Cities in Mountain Area (Chongqing University), Ministry of Education, Chongqing 400030, China*

Correspondence should be addressed to Yu Yu; cquyuy@163.com

Received 6 February 2018; Revised 23 July 2018; Accepted 7 August 2018; Published 12 September 2018

Academic Editor: Farhad Aslani

Four test pieces with different steel plate center-to-center distances and reinforcement ratios are subjected to low-cycle repeat quasistatic loading to optimize properties as failure mode, hysteretic curve, skeleton curve, energy dissipation parameters, strength parameters, and seismic performance of high-strength concrete low-rise shear walls. The embedded steel plates are shown to effectively restrict wall crack propagation, enhance the overall steel ratio, and improve the failure mode of the wall while reducing the degree of brittle failure. Under the same conditions, increasing the spacing between the steel plates in the steel plate concrete shear wall can effectively preserve the horizontal bearing capacity of the shear wall under an ultimate load. The embedded steel plates perform better than concealed bracing in delaying stiffness degeneration in the low-rise shear walls, thus safeguarding their long-term bearing capacity. The results presented here may provide a workable basis for shear wall design optimization.

1. Introduction

Shear walls are lateral-force-resistant components commonly found in framework-wall and framework-core tube structures. Under seismic action, the shear wall bears the majority of the horizontal force acting on the structure per its high lateral stiffness. Most reinforced concrete shear walls crack easily, which leads to rapid degradation of the horizontal bearing capacity, ductility, and dissipation of seismic energy. The axial force of bottom shear walls also increases as building height increases. The axial compression ratio of common reinforced concrete shear walls can only be controlled by increasing the wall thickness or improving the concrete grade to enhance the ductility and energy dissipation capacity of the shear walls. However, increasing the wall thickness can create space-utilization and construction problems, increase the structural dead load, and cause excessive high lateral stiffness, among other issues. Increasing the concrete grade also influences the shear wall ductility. Optimizing the common reinforced concrete shear wall is a challenging, though crucial design factor in super high-rise building structures.

Previous researchers have extensively investigated composite structures of steel plate concrete shear walls. Driver et al. [1], for example, studied the seismic performance of composite shear walls of four-layer steel plate concrete via low-cycle repeated horizontal loading test; they found that such walls have a high ductility, excellent energy dissipation capacity, and high lateral stiffness. Tong et al. [2] studied the bearing capacity of steel frame-steel plate concrete composite shear walls, including shearing studs, without vertical loading in a low-cycle repeated pseudostatic test; the shearing studs proved highly effective under these conditions, but did begin to yield upon cracking of the shear wall. The bearing capacity of the composite shear wall containing a steel frame-steel plate concrete decreases rapidly in the late loading stage.

There have been many other valuable contributions to the literature. Arabzadeh et al. [3] conducted a model test on a three-layer steel frame-plate composite shear wall at a 1 : 3 reduced scale to find that enclosed concrete slabs can effectively limit the out-of-plane buckling deformation of thin steel plates and improve the ductility and energy dissipation of the wall structure. Mun et al. [4] studied the shearing

properties of heavy-duty shear walls; Marsono and Hatami [5] analyzed and studied the octagonal single-reinforcement concrete shear walls. Chen et al. [6] investigated a composite system of reinforced concrete and shear walls. Mohebbi et al. [7] explored the seismic performance of the cold-rolled shear walls, and Peng et al. [8] studied the properties of a precast concrete shear wall under a cyclic load. Gorji and Cheng [9] studied performance-based design of coupled steel plate shear walls according to plastic analysis. Tian et al. [10] developed a new structural system called steel frame with cold-formed steel shear infill walls. Zhai et al. [11] found that the shear capacity, shear stiffness, and shear slip increased significantly with the increase of tie-bar diameter. Aghayari and Dardaei [12] discussed the behavior of reinforced concrete frames braced with steel shear walls investigated and compared with other medium and high-strength steel with different thicknesses. Dar et al. [13] presented various innovative sectional profiles and stiffening arrangements for cold-formed steel beams contributing in delaying or eliminating various modes of premature buckling. Borzoo et al. [14] used finite element analysis to evaluate the stiffness, strength, and failure mode at cold-formed steel shear panels whit steel sheathing.

In the present study, we simulated seismic action with low-cycle repeated loading and observed crack development and deformation in a series of shear wall test pieces. We plotted hysteretic and skeleton curves for the test pieces according to the test data to assess various characteristics of the test pieces (e.g., energy dissipation and intensity attenuation). We sought to determine the seismic performance of an oblique section of the high-strength concrete low-rise shear wall, as discussed below.

2. Test Overview

2.1. Test Design

2.1.1. Test Piece Design. We used a 1/4 reduced scale to design our test pieces according to *Technical specification for seismic tests of buildings* (JGJ101-2015) [15]. The external dimensions of the four test pieces are the same as those of SRHCW-2 (SRHCW is the abbreviation of steel reinforced high-strength concrete wall); their sectional dimensions are 120×800 mm and shear span ratio is $\lambda = 1$, as shown in Figure 1. All axial compression ratios were set to 0.40 per the requirements of mid- and high-rise building shear walls in high seismic intensity regions.

The four test pieces have the same wall reinforcement, edge component section steel and reinforcement properties, and loading beam and support reinforcement; they were given different center-to-center distances between steel plates and different steel ratios in the plates. The uniform parameters include horizontally distributed reinforcing bar reinforcement ratio of 0.276%, vertically distributed reinforcing bar reinforcement ratio of 0.346%, edge component length of $0.2L$, 160 mm (in which L is the cross section's height of shear wall), edge component longitudinal reinforcing bar reinforcement ratio of 1.57%, cold-rolled edge component section steel ratio of 1.32%, and edge component volume stirrup reinforcement ratio of 1.20%.

The test pieces were numbered as follows: SPRCW-5 (steel plate ratio 1.0%; center-to-center distance between steel plates, 330 mm); SPRCW-6 (steel plate ratio 1.0%; center-to-center distance between steel plates, 180 mm); SPRCW-7 (steel plate ratio 1.6%; center-to-center distance between steel plates, 330 mm); SPRCW-8 (steel plate ratio 1.6%; center-to-center distance between steel plates, 180 mm). Table 1 and Figure 2 provide detailed dimension and reinforcement parameters of SRHCW-2 and SPRCW-5 (SPRCW is the abbreviation of steel plate reinforced concrete wall).

Shearing studs were welded onto both surfaces of the hot-rolled steel plate to prevent early out-of-plane buckling in the plate or early binding-slippage between the plate and concrete and to guarantee effective incorporation between the plates and concrete. The intrinsic shear of the studs reduces the interactive force between the steel plate and concrete surface to prevent early binding-slippage, while the bending of the shearing studs limits out-of-plane deformation of the steel plate and improves the seismic performance of the steel plate concrete shear wall.

2.1.2. Concrete Preparation. We used C60 high-strength concrete in the test with mix ratios shown in Table 2.

2.1.3. Steel Mechanical Properties. The steel walls we tested include A6.5 vertically distributed reinforcing bars and horizontally distributed reinforcing bars, A8 vertical tensioned bars as edge components, steel plates with 6.0 mm thickness, and channel steel with 2.2 mm thickness. All reinforcing bars are HPB300 hot-rolled reinforcing bars and plates are Q235 hot-rolled steel. The edge component channel steel is cold-rolled thin-wall sections.

Test pieces were sampled and processed according to the *Technical specification for tensile test of metal materials at room temperature* (GB/T 228-2010) [16]. Table 3 shows the mechanical properties of steel as determined by material property tests.

2.1.4. Measured Strength of Concrete and Axial Compression of Test Pieces. All four test pieces, as mentioned above, are comprised of concrete with a strength grade of C60. The test pieces were prepared by concrete placement in two batches with two test pieces in each batch to control the differences in concrete strength among the four pieces. The measured standard value of concrete strength $f_{cu,k}$ is the mean of the measured values of compressive strength of 3×150 mm standard cubes prepared by concrete placement at the time when the test pieces were prepared, as shown in Table 4; f_c is the concrete compressive strength design value, f_t is the concrete tensile strength design value, and N_t is the loading axial force in the test.

2.2. Test Devices and Loading System

2.2.1. Test Devices. We ran a horizontal low-cycle repeat quasistatic loading test according to *Technical specification*

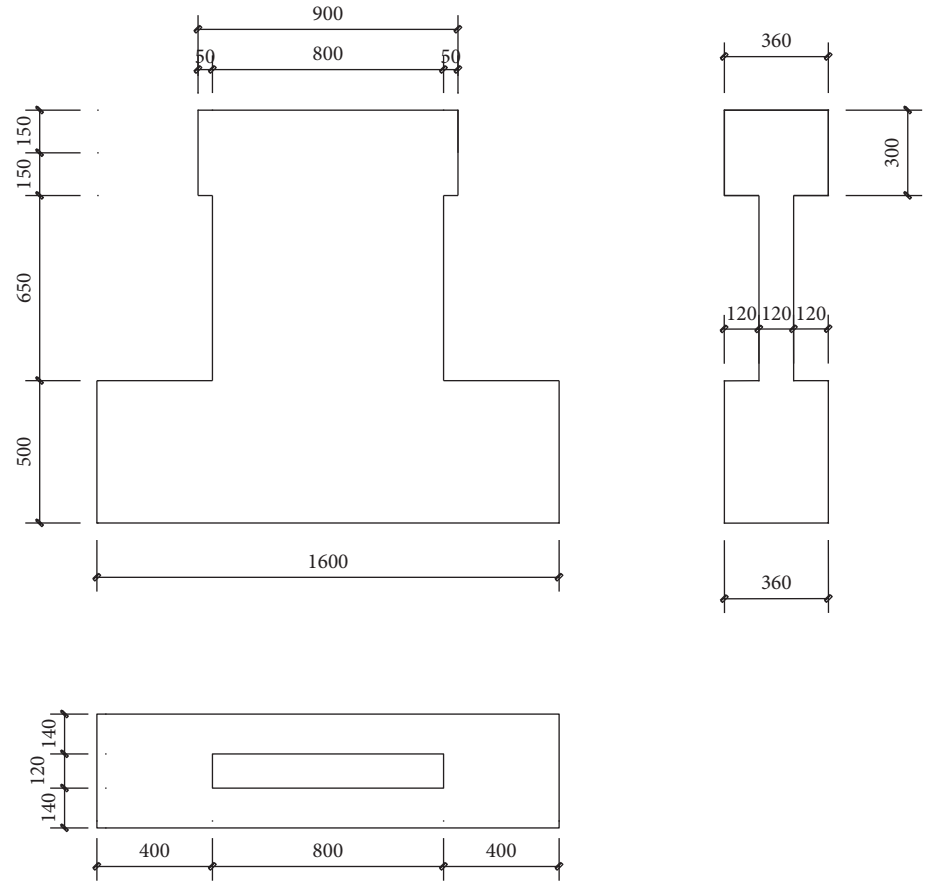

Figure 1: Test piece dimensions.

Table 1: Test piece parameters.

Parameters	Test piece number			
	SPRCW-5	SPRCW-6	SPRCW-7	SPRCW-8
Wall				
Wall thickness, bw (mm)	120	120	120	120
Wall width, L (mm)	800	800	800	800
Wall clear height, Hn (mm)	650	650	650	650
Shear span ratio	1	1	1	1
Edge component, bw × Lc (mm)	120 × 160	120 × 160	120 × 160	120 × 160
Edge component height (mm)	800	800	800	800
Horizontally distributed reinforcing bars in wall-②	A6.5 @ 200	A6.5 @ 200	A6.5 @ 200	A6.5 @ 200
Reinforcement ratio of horizontally distributed reinforcing bars (%)	0.276	0.276	0.276	0.276
Vertically distributed reinforcing bars in wall-⑧	A6.5 @ 160	A6.5 @ 160	A6.5 @ 160	A6.5 @ 160
Reinforcement ratio of vertically distributed reinforcing bars (%)	0.346	0.346	0.346	0.346
Main reinforcing bars of edge components-⑬	6A8	6A8	6A8	6A8
Section steel of edge components-⑨	[60 × 30 × 2.2]	[60 × 30 × 2.2]	[60 × 30 × 2.2]	[60 × 30 × 2.2]
Stirrups of edge components-①	A6.5 @ 100	A6.5 @ 100	A6.5 @ 100	A6.5 @ 100
Cross section of concealed bracing	—	—	—	—
Cross section of steel plate-⑪	**80 × 6**	**80 × 6**	**128 × 6**	**128 × 6**
Steel ratio of steel plate (%)	**1.0**	**1.0**	**1.6**	**1.6**
Center-to-center distance between steel plates S_2 (mm)	**330**	**180**	**330**	**180**

Table 1: Continued.

Parameters	Test piece number			
	SPRCW-5	SPRCW-6	SPRCW-7	SPRCW-8
Loading beam				
Length, L_1 (mm)	900	900	900	900
Width, B_1 (mm)	300	300	300	300
Height, H_1 (mm)	300	300	300	300
Main reinforcing bars-⑤	4C20	4C20	4C20	4C20
Stirrup-③	A8 @ 100	A8 @ 100	A8 @ 100	A8 @ 100
Support beam				
Length, L_2 (mm)	1600	1600	1600	1600
Width, B_2 (mm)	400	400	400	400
Height, H_2 (mm)	500	500	500	500
Main reinforcing bars-⑦	8C20	8C20	8C20	8C20
Stirrup-⑥	A8 @ 100	A8 @ 100	A8 @ 100	A8 @ 100

Note: Steel plate ratio of SRHCW-2 concealed bracing and vertically distributed reinforcing bar is 1.04%. A is HPB300 steel and C is HRB400 steel. The height of the edge component is equal to Hn + H_1/2. The diameter of the pin is 10 mm, the length is 25 mm, and the material performance grade is 4.6.

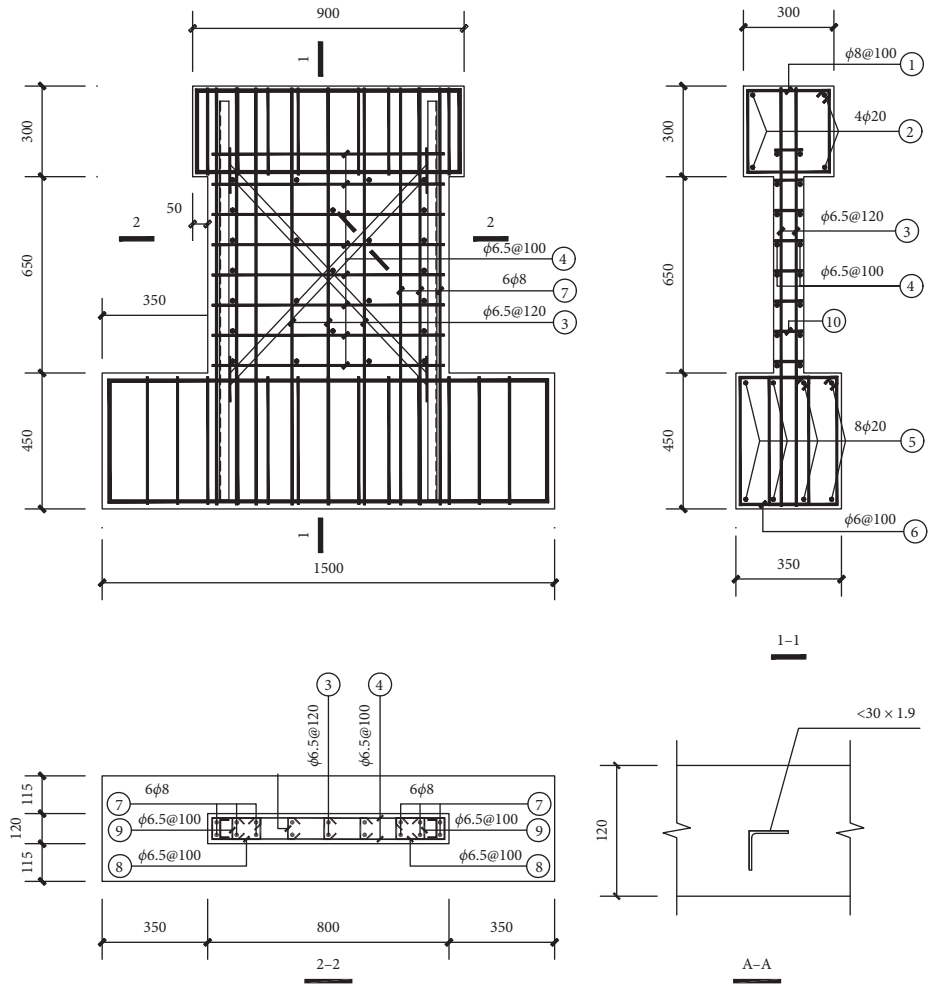

(a)

Figure 2: Continued.

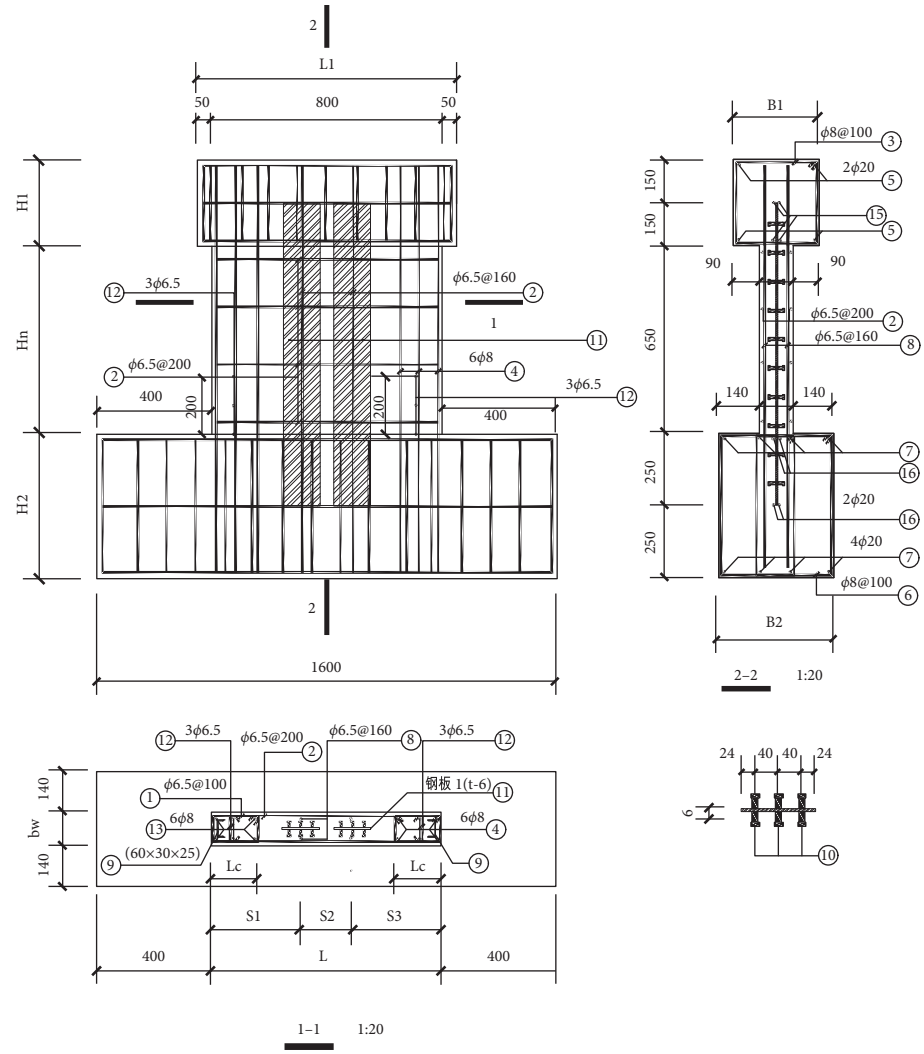

(b)

Figure 2: Construction drawing. (a) SRHCW-2 specimen. (b) SPRCW-5 specimen.

Table 2: C60 concrete mix ratio.

Material components	Gravel	Sand	R42.5 cement	Coal ash	Water	Polycarboxylic acid water reducer
Mix ratio	1.85	0.90	1.00	0.08	0.26	0.01
kg/m^3	1119	546	602	50	165	7.5

Table 3: Steel performance parameters.

Steel type		Elasticity modulus (MPa)	Yield strain ($\mu\varepsilon$)	Yield strength (MPa)	Ultimate strength (MPa)
Steel plate (mm)	6.0	202043.2	1498.7	302.8	450.1
Cold-rolled section steel (mm)	2.2	212491.7	1808.1	384.2	414.1
Reinforcing bar (mm)	A6.5	254633.7	1645.5	419.0	607.7
	A8.0	201135.0	1637.2	329.3	494.7

for seismic tests of buildings (JGJ101-2015) [15]. Loads were applied vertically and horizontally in respective sets. The vertical load was kept stable throughout the experiment as applied on the loading beam by a vertical oil jack. The horizontal load was applied on the loading beam by a horizontal actuator with one end hinged to a horizontal connecting device and the other end fixed to the reaction wall, which balanced the horizontal counter-force. The loading devices mainly include a reaction beam, vertical oil jack, and jack pulley. The foundation beam of each test piece

Table 4: Measured strength of concrete and vertical loads of test pieces.

Test piece number	Design axial compression ratio	Experiment-al axial compression ratio	$f_{cu,k}$ (MPa)	f_c (MPa)	f_t (MPa)	N_t (kN)
SRHCW-2	0.52	0.24	59.3	27.2	2.40	1140
SPRCW-5	0.40	0.18	58.3	26.8	2.01	857
SPRCW-6	0.40	0.18	55.7	25.6	1.98	819
SPRCW-7	0.40	0.18	58.3	26.8	2.01	857
SPRCW-8	0.40	0.18	55.7	25.6	1.98	819

was fixed by connecting the anchor bolts into laboratory grooves. Four jacks and horizontal supports were used to support both ends of the base beam to prevent any experimental error due to sliding of the test pieces during the loading process. Figure 3 shows a diagram of the loading devices.

2.2.2. Test Loading System. We applied low-cycle repeat quasistatic loading in the tests, as discussed above. Axial compression was maintained at the preset value while horizontal force was changed continuously according to the loading system. Force control was imposed before cracking of the test pieces and displacement control was imposed after cracking. The specific loading process was as follows according to *Technical specification for seismic tests of buildings* (JGJ101-2015) [15].

(1) In the preloading stage, a 150 kN vertical load was applied on the top of the loading beam before decreasing the load to 0 kN to eliminate nonuniformity in the internal organization of the concrete, and this step was repeated twice. The load was then increased to the preset value N_t at three levels. This value remained unchanged during the test. The horizontal repeated load was preloaded after the vertical load was preloaded. Microcycling was performed with a horizontal force of $20\,\text{kN} \rightarrow 0 \rightarrow -20\,\text{kN}$ to verify the operative mode, instrument connection, data box, and other relevant factors of the test devices for normal operation.

(2) We applied a forward horizontal load on the horizontal actuator in the force control loading stage. The load was gradually increased from 20 kN to 160 kN with a 20 kN gradient, then at a 10 kN gradient until cracks appeared in the test pieces. The cracks and cracking loads P_{cr} were recorded immediately. The horizontal force was unloaded to 0 kN at three levels. The backward cracking load P_{cr} was determined in the same stepwise process and the cracks recorded similarly.

(3) In the next stage, displacement loading was applied once cracks occurred in test pieces. The initial position of each test piece was the 0 mm point after the application of axial force. Loading was performed according to the wall top control displacement, and the displacement at each level was repeated twice. Loading and unloading were completed uniformly in three segments according to the displacement value in the first cycle; loading and unloading were completed a single time in the second cycle. Forward and backward control displacement was alternatively loaded, and loading and unloading were carefully kept smooth and continuous. The test was not finished until the horizontal bearing capacity of test pieces decreased to 85% of the ultimate bearing capacity or the test pieces lost their vertical bearing capacity. The wall top control displacements were 0.9 mm, 1.5 mm, 2.1 mm, 3.0 mm, 4.0 mm, 5.0 mm, 6.6 mm, 8.0 mm, 10.0 mm, 13.0 mm, 15.0 mm, and 18.0 mm, respectively (Figure 4).

2.3. Measuring Point Layout. We used four components of identical dimensions in the test. The cold-rolled thin-wall section steel and reinforcing bars have the same layout, so the positions of strain gages were consistent among the four test pieces. The lower middle part of the steel plate was subjected to a strong force which easily bent it, so we placed a strain rosette in the lower middle part of the plate to monitor changes in strain. The specific layout of displacement meters, strain gages, and strain rosettes is shown in Figure 5. Figure 6 is the test specimen before pouring concrete.

3. Test Results

3.1. Test Piece Failure Mode Analysis. The failure types of common reinforced concrete shear walls can be divided into three types by shear span ratio. The failure type of low-rise shear walls with a shear span ratio $\lambda \leq 1$ is generally shearing failure. The medium and high shear failure type with $1 < \lambda < 2$ is generally bending-shear failure. High shear walls with a shear span ratio $\lambda > 2$ are generally bending failure. The failure types of steel plate concrete shear walls can be classified according to known features of common steel plate concrete shear walls. Our four test pieces had the same shear span ratio, 1.0, and thus belong to the low-rise shear wall category. The failure types of test pieces were determined according to changes in their bearing capacity, crack development mode, and final failure mode. Figures 7–10 show the wall failure modes of our test pieces.

The test piece SPRCW-5 experienced 15 displacement loading cycles in total from loading to failure. The first cycle was finished when the wall top displacement Δ had increased to 8.0 mm. The horizontal bearing capacity of SPRCW-5 decreased rapidly after it reached this maximum point. The vertical bearing capacity decreased rapidly upon failure, which indicates significant brittle failure characteristics.

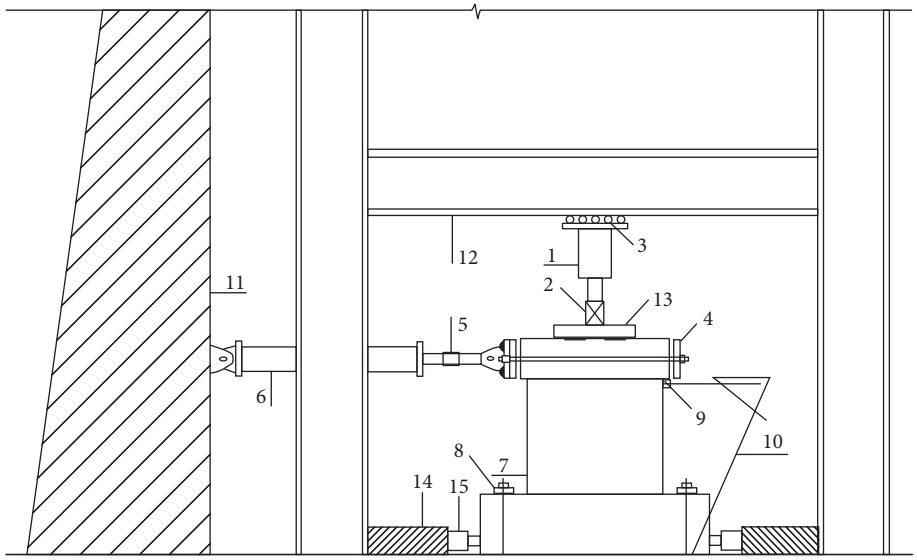

Figure 3: Loading device. (1) 150T vertical oil Jack; (2) 150T vertical sensor; (3) sliding support; (4) horizontally connected device; (5) 150T horizontal sensor; (6) 150T horizontal actuator; (7) test piece; (8) anchor bolt; (9) displacement meter; (10) slotted-angle shelving; (11) reaction wall; (12) reaction beam; (13) distribution beam; (14) support; (15) 30T Jack.

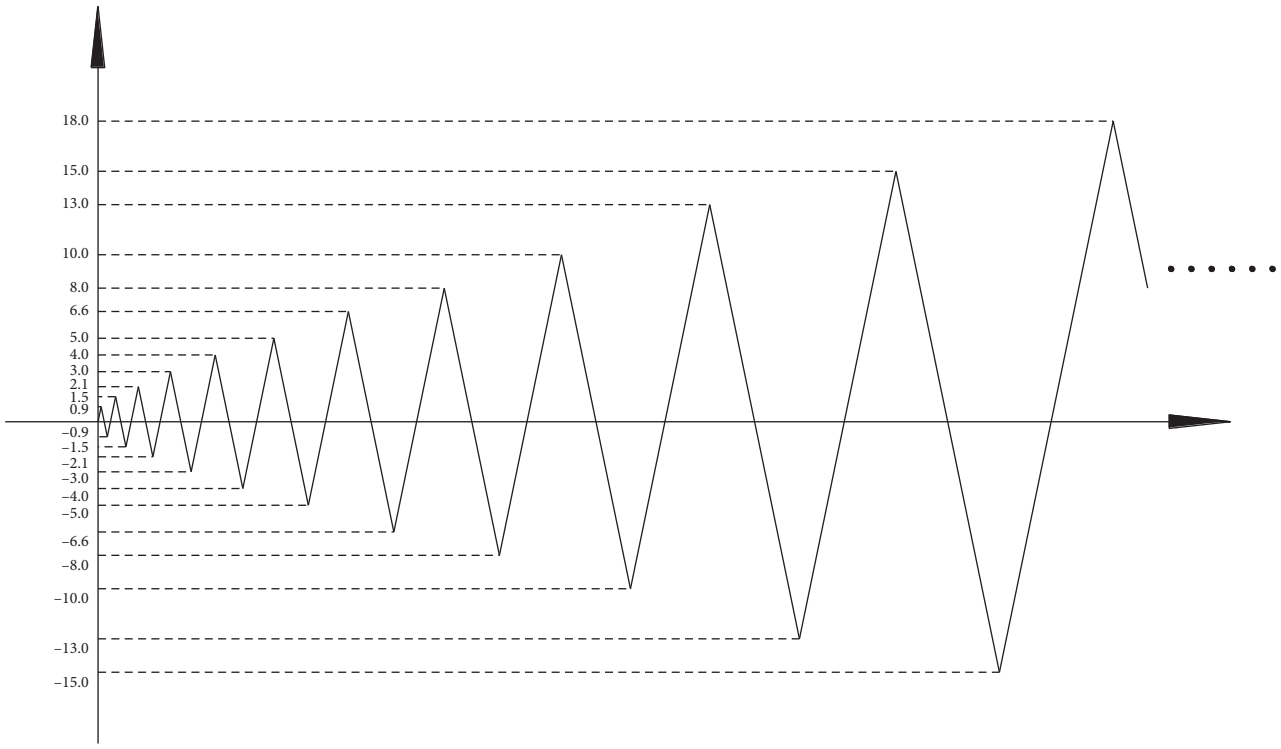

Figure 4: Displacement control loading velocity.

Cracks developed in various parts of the wall, mostly along the diagonal line of the wall. No wide principal oblique cracks formed before failure. Most cracks were thin, short, and oblique. No severe binding-slippage occurred between the steel plate and the concrete, so the resulting hysteretic curve was plump in shape.

In the later stage of crack development, the lower left and lower right parts of the wall split the concrete to create a small-range, diagonal compression strut area. The forward and backward cracks in the middle part split the concrete into fine and tiny concrete blocks and ultimately crushed the diagonal compression strut. The longitudinal bars in the corner and the section steel were raised, and concrete blocks were raised in the area where the central forward and backward cracks joined. The wall was fragmented; the steel plate lost its out-of-plane restriction and bent. The test piece

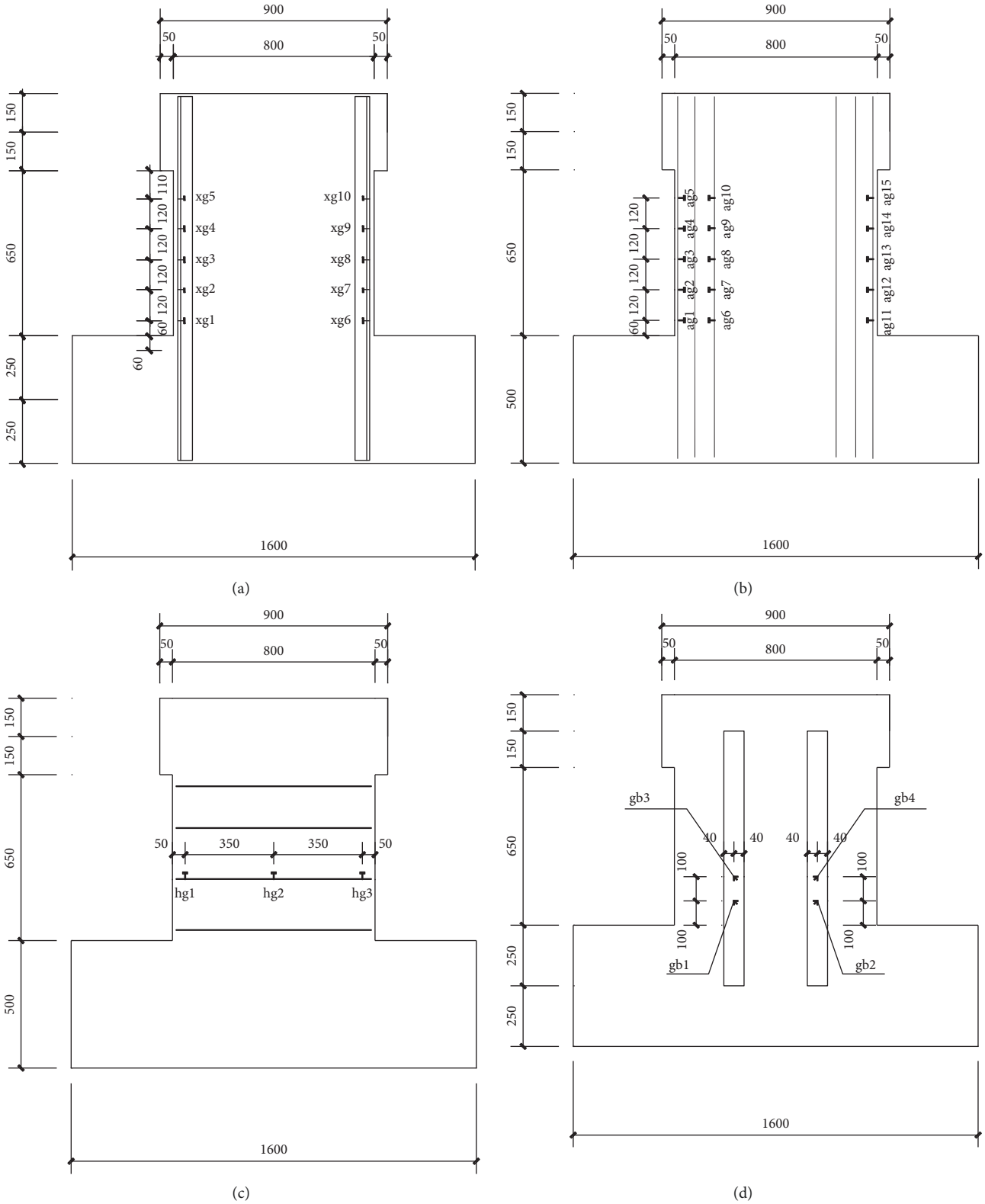

Figure 5: Continued.

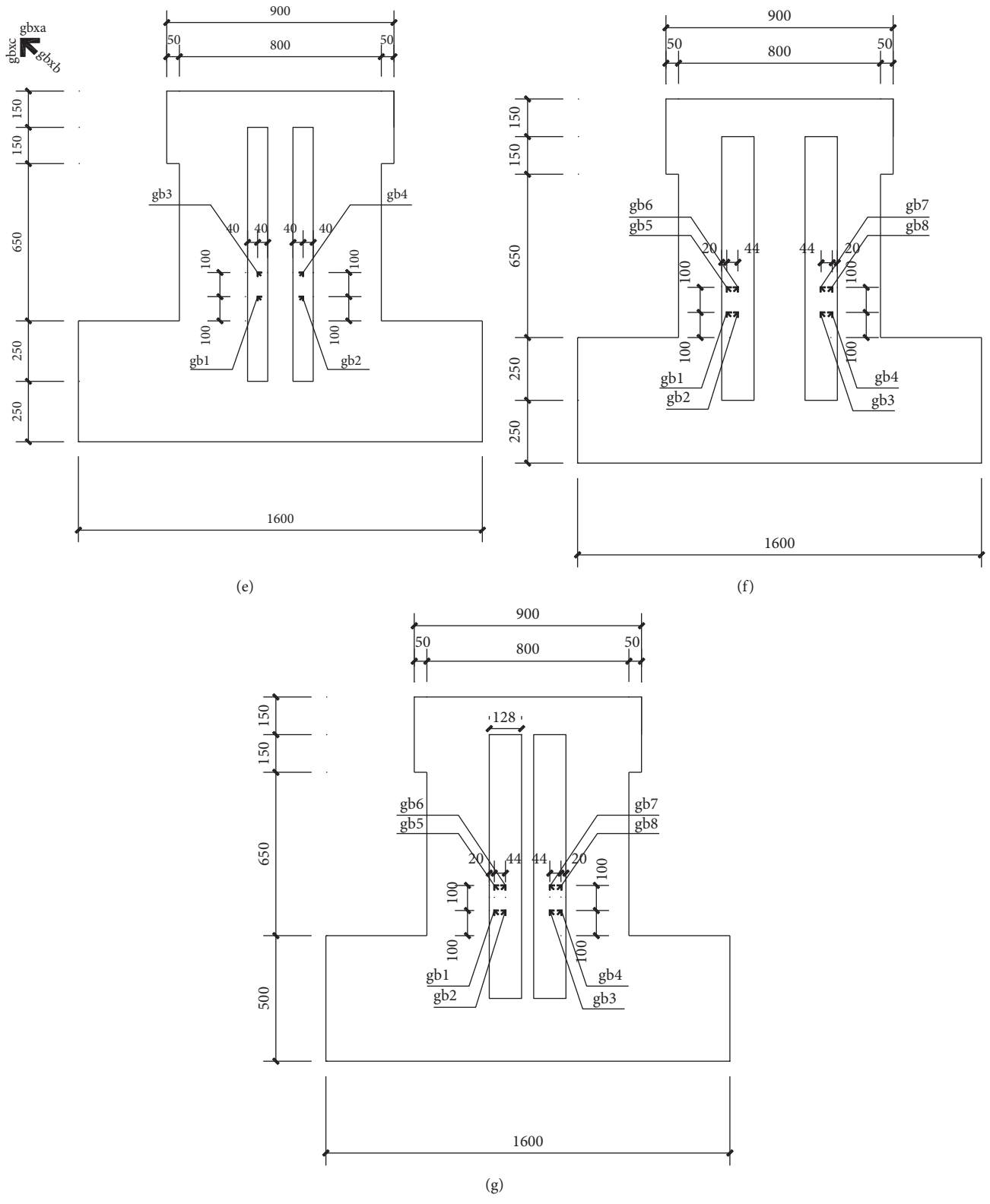

Figure 5: Strain measuring point layouts. (a) Cold-rolled section steel strain measuring points. (b) Edge component longitudinal bar strain measuring points. (c) Horizontally distributed bar strain measuring points. (d) SPRCW-5 steel plate strain measuring points. (e) SPRCW-6 steel plate strain measuring points. (f) SPRCW-7 steel plate strain measuring points. (g) SPRCW-8 steel plate strain measuring points.

rapidly lost vertical and horizontal bearing capacity and failed. SPRCW-5 showed significant brittle failure characteristics and shearing failure type.

SPRCW-6 experienced 16 displacement loading cycles in total from loading to failure. The test piece failed when the wall top displacement Δ had increased to 8.0 mm in the

(a) (b)

Figure 6: Test specimen before pouring concrete.

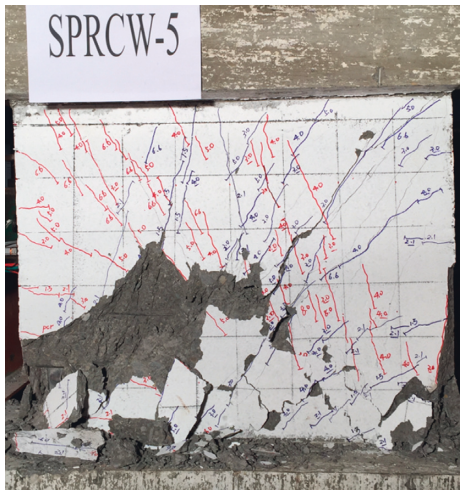

Figure 7: Failure mode of SPRCW-5.

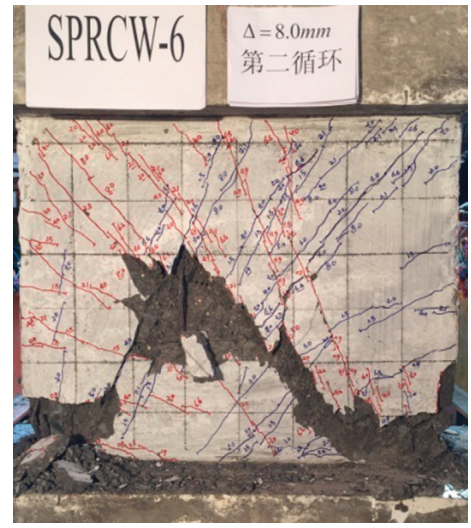

Figure 8: Failure mode of SPRCW-6.

second cycle. The horizontal bearing capacity of SPRCW-6 rapidly decreased in the late loading stage. The test piece rapidly lost its vertical bearing capacity upon failure, exhibiting significant brittle failure characteristics. Cracks developed in various parts of the wall; most oblique cracks were distributed in the vicinity of the diagonal line of the wall. No main oblique cracks extended through the whole wall before failure. The crack width was small, indicating that no severe binding-slippage had occurred between the steel plate and concrete.

Cracks in the vicinity of the diagonal line of the wall split the concrete into several diagonal compression concrete columns at a 45° angle. In the late loading stage, many thin and short compression cracks occurred in the diagonal compression concrete columns in lower half of the wall. The diagonal compression concrete columns were crushed, and the wall was fragmented; the failure area was splay-shaped. After the concrete in the middle part of wall was raised and detached, the steel plate was bent and raised due to loss of the restriction from the external concrete. The test pieces rapidly lost vertical and horizontal bearing capacity and failed. The failure mode of SPRCW-6 exhibited significant brittleness, and the failure type was shearing.

The test piece SPRCW-7 experienced 19 displacement loading cycles in total from loading to failure. The test piece failed when the wall top displacement Δ had increased to 13.0 mm in the first cycle. The horizontal bearing capacity of SPRCW-7 remained at about 93% of its peak until failure rather than decreasing in the late loading stage, so the failure mode of this test piece appears to include bending. The test piece suddenly lost horizontal bearing capacity when it

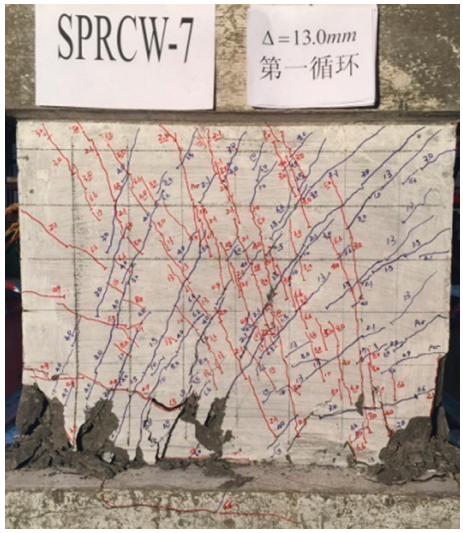

Figure 9: Failure mode of SPRCW-7.

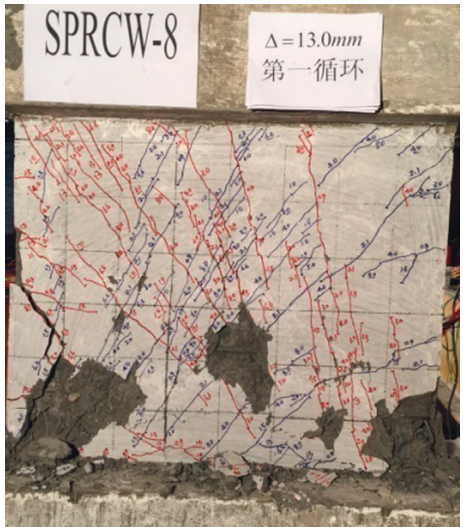

Figure 10: Failure mode of SPRCW-8.

failed. The vertical bearing capacity decreased by about 20%, exhibiting brittle failure characteristics and indicating shear failure as well. The wall cracks were parallel to the diagonal line, fully developed, and extensively distributed. There were a few cracks on the wall edge. The cracks concentrated in the other positions had relatively small width. The oblique cracks split the concrete into a large number of concrete diagonal compression struts. The cracks in the wall corner were thin and short, thus forming dense compression struts. The concrete compression struts in the wall corner were first crushed during the loading process, and then struts in the lower left and lower right parts were fragmented into concrete blocks due to repeated tension and compression; they were raised and detached from the wall immediately. The edge component section steel and longitudinal bars were bent and raised. The crushing area of the concrete in the wall corner increased throughout the test. Finally, the cross section of wall bottom failed under the shearing force as it was unable to resist the horizontal force. The wall was complete when it failed. The failure mode of SPRCW-7 includes both bending failure and shear failure, so its type is bending-shear failure.

The test piece SPRCW-8 experienced 19 displacement loading cycles in total from loading to failure. The test piece failed in the first cycle when the wall top displacement Δ had increased to 13.0 mm. The horizontal bearing capacity of SPRCW-8 decreased slowly after it reached the peak. It suddenly failed and lost horizontal bearing capacity entirely once said capacity decreased to about 50% of the peak. The vertical bearing capacity decreased by about 30%. The test piece exhibited both bending failure characteristics and brittleness characteristics of shear failure when it failed. Wall cracks developed parallel to the diagonal line and were dense in the middle part with relatively small width. Cracks were found in all positions of the wall. No principal oblique crack penetrating the wall was found, so no severe binding-slippage occurred between the steel plate and concrete.

Oblique cracks of the wall split the concrete into a large number of thin and short concrete diagonal compression struts. A large number of fragmented concrete blocks formed at the point where the forward and backward cracks joined. The concrete in the wall corner was first crushed, and the range of the crushed area increased continuously. The concrete in the crushed area was immediately raised and detached from the wall under repeated tension and compression. The lower left and lower right concrete diagonal compression struts were then fragmented into concrete blocks under repeated tension and compression and immediately raised and detached from the wall. The lower middle fragmented concrete blocks were also continuously raised and detached from the wall. The lower cross section of the wall was weakened continuously and ultimately failed under the shear force. The failure mode of SPRCW-8 included both bending failure and shear failure, so its failure type is bending-shear failure.

Based on a comparative analysis of the failure modes of the four test pieces, the shearing studs did effectively limit binding-slippage between the steel plate and concrete thus restricting oblique crack widening. The tensile and shearing properties of the steel plates also effectively limited the extension and widening of cracks. The failure type of the SPRCW-5 and SPRCW-6 test pieces was shear. The failure type of the SPRCW-7 and SPRCW-8 test pieces, which have a higher steel ratio, was bending-shear. To this effect, increasing the steel plate ratio effectively improved the failure type of low-rise shear walls by enabling a transition from significant brittleness to high ductility. The relative completeness of the wall in the case of failure was also retained under these conditions, which improved the safety of the shear wall.

3.2. Hysteretic Curves of Test Pieces. Hysteretic curves allow for comprehensive analysis of the seismic performance of test pieces under the action of low-cycle repeat horizontal force. The area enclosed by the hysteretic curve is the energy dissipated during the low-cycle repeat loading process, so the energy dissipation capacity of each test piece can be judged according to the curve shape. The changes in peak

force and displacement in each cycle reflect stiffness degeneration, bearing capacity attenuation, deformability, and ductility in each test piece during the loading process. Based on the hysteretic curves recorded by the X-Y function recorder, we digitally processed the manually recorded horizontal force and displacement data to obtain the hysteretic curves shown in Figure 11.

The hysteretic curves of the five test pieces, SPRCW-5-8 and SRHCW-2, showed several similarities and differences. All test pieces were in an elastic state before cracking. The unloading curve returned to the origin, and the loading and unloading curves nearly coincided, which indicates that no plastic deformation occurred at this point. Once the test piece cracked and bent, the area enveloped by the hysteretic curve was small. The residue deformation was very small when the horizontal force was unloaded to 0 kN. The horizontal bearing capacity increased as displacement increased. There are no significant differences in the hysteretic curve between the first and second cycles, suggesting that this stage contained a small percentage of plastic deformation and was dominated by elastic deformation. The wall rigidity did not deteriorate. Thus, greater displacement caused an increase in horizontal bearing capacity.

The envelope area of the hysteretic curve increased as horizontal displacement increased after the test piece was yielded. The residual deformation also increased when the horizontal force decreased to 0 kN, which indicates that a percentage of plastic deformation in the test piece had increased as well as the energy dissipated in each cycle. The horizontal bearing capacity of the test piece decreased to some extent as displacement increased after reaching the peak, indicating that the rigidity of the test piece decreased with increase in the percentage of plastic deformation. Differences in the envelope area of the hysteretic curve and the peak of horizontal bearing capacity between the first and second cycles also increased as displacement increased, which indicates that cracks developed continuously and that internal structural damage grew increasingly severe when the test pieces were yielded.

Pieces SPRCW-5-8 had arch-shaped hysteretic curves with less significant rheostriction effect than SRHCW-2, indicating that no severe binding-slippage occurred between the steel plate and concrete after the four test pieces cracked in the test. The shearing studs welded onto both surfaces of the steel plate apparently did effectively limit the binding-slippage between the steel plate and concrete and enhanced the energy dissipation performance of the low-rise shear wall. The embedding of steel plates also effectively improved the plastic deformation of the wall and absorbed seismic energy better than concealed bracing.

The horizontal bearing capacity of SPRCW-7 and SPRCW-8 decreased at a much lower rate than SPRCW-5 or SPRCW-6 upon reaching the ultimate load. The latter exhibited significant brittle failure characteristics, as well; the former two failed only after the displacement reached 13 mm while the latter two failed just after the displacement reached 8 mm. The steel ratios of the former two were higher than that of the latter two. Increasing the steel ratio of the steel plate concrete shear wall under the same conditions appears to significantly increase the ultimate displacement of the shear wall and delay the intensity attenuation in the wall.

SPRCW-7 and SPRCW-8 had a plumper hysteretic curve and a larger envelop area than SPRCW-5 or SPRCW-6. Such differences were more significant after the test pieces were yielded. It seems that increasing the steel plate ratio in the steel plate concrete shear wall under the same conditions effectively improves the energy dissipation capacity of the wall.

Based on a comparison of the hysteretic curves of SPRCW-7 and SPRCW-8, we found that horizontal bearing capacity increased as displacement increased but remained fairly stable when SPRCW-7 reached its ultimate load. The horizontal bearing capacity of SPRCW-8 decreased to some extent with displacement when SPRCW-8 reached its peak. SPRCW-7 and SPRCW-8 had different center-to-center distances of steel plates, as mentioned above: that of SPRCW-7 was 330 mm; i.e., the steel plates were closer to the edge components. The center-to-center distance of steel plates in SPRCW-8 was 180 mm. Increasing the spacing between steel plates in the steel plate concrete shear wall under the same conditions appears to effectively delay the decrease in horizontal bearing capacity in the wall upon reaching the ultimate load.

3.3. Skeleton Curves of Test Pieces. We plotted skeleton curves by smoothly connecting all points of maximum horizontal force larger than that applied previously in the force-displacement curves in the same loading direction (pushing or pulling). As a locus curve of the maximum horizontal load in each cycle, the skeleton curve directly reflects the force and deformation characteristics of the test pieces in different stages. These curves allowed us to directly compare the rigidity, strength, energy dissipation capacity, and ductility among different test pieces. The skeleton curves of SPRCW-5-SPRCW-8 and SRHCW-2 are shown in Figure 12.

The skeleton curves feature several notable characteristics. The skeleton curves of the four components were in a straight-line state before cracking, indicating that the rigidity of the test pieces did not deteriorate before cracking and that they remained in an elastic-elastic stage. The straight-line segments of the skeleton curves of the components nearly coincide, indicating only very slight differences in initial rigidity among the four test pieces. It was thus clear that the steel plate spacing and steel ratio of the steel plate had little effect on the initial rigidity of the low-rise shear wall. The rigidity of the test pieces began to deteriorate after cracking and was decreased as displacement increased.

When steel plate spacing was constant, the descending slopes of the horizontal bearing capacity of SPRCW-7 and SPRCW-8 were gentler than those of SPRCW-5 and SPRCW-6 upon reaching the ultimate load. In addition, the ultimate displacements of SPRCW-7 and SPRCW-8 were larger than that of SPRCW-5 and SPRCW-6 upon failure. Apparently, increasing the steel ratio in the plate under the same conditions effectively slows down the decrease in horizontal bearing capacity upon ultimate load.

When steel ratio was constant, the horizontal bearing capacity of SPRCW-5 was decreased at a slightly slower rate than SPRCW-6 after the peak was reached; the displacements

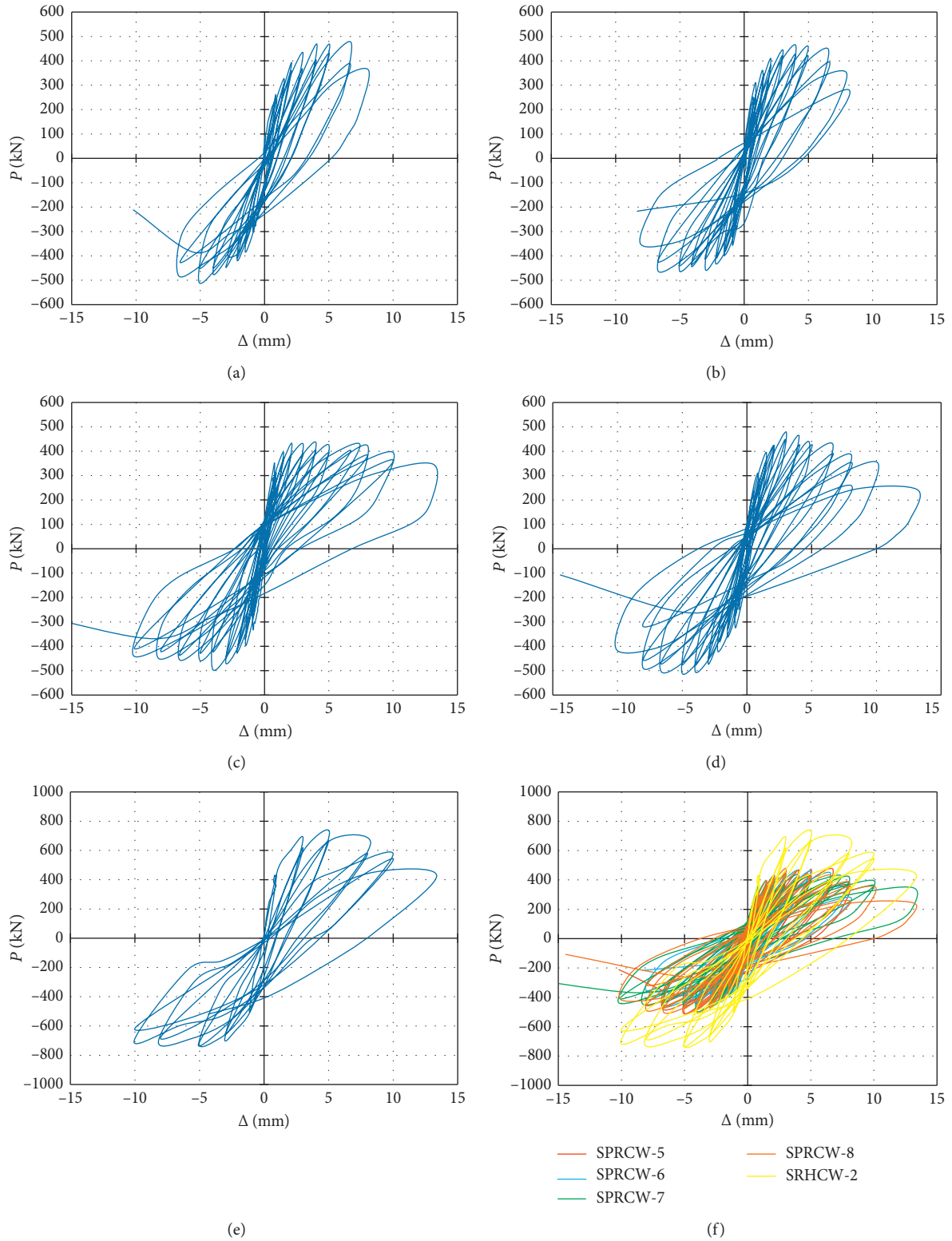

Figure 11: Hysteretic curves of shear wall test pieces. (a) SPRCW-5 P-Δ hysteretic curve. (b) SPRCW-6 P-Δ hysteretic curve. (c) SPRCW-7 P-Δ hysteretic curve. (d) SPRCW-8 P-Δ hysteretic curve. (e) SRHCW-2 P-Δ hysteretic curve. (f) Hysteretic curves of all test pieces.

loaded during failure were the same. The horizontal bearing capacity of SPRCW-7 did not decrease immediately after the ultimate load was reached; instead, its skeleton curve gradually decreased only after a long plateau. The horizontal bearing capacity of SPRCW-8, conversely, began a quick descent upon reaching the ultimate load and its skeleton curve had no plateau. The displacements loaded during failure were, again, equal. Increasing the steel plate spacing under the same

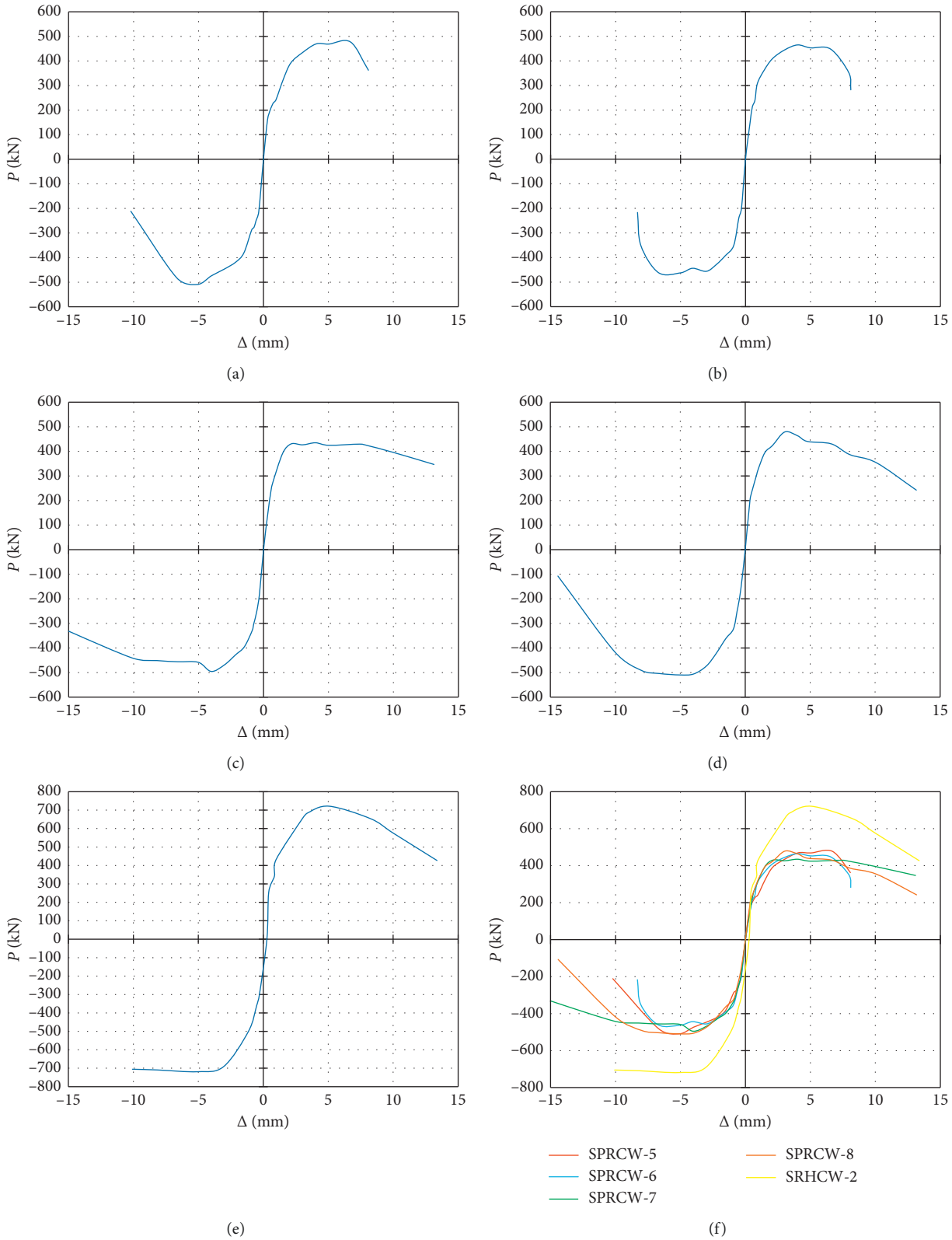

Figure 12: Skeleton curves of shear wall test pieces. (a) Skeleton curve of SPRCW-5. (b) Skeleton curve of SPRCW-6. (c) Skeleton curve of SPRCW-7. (d) Skeleton curve of SPRCW-8. (e) Skeleton curve of SRHCW-2. (f) Skeleton curves of all test pieces.

conditions appears to slightly decelerate horizontal bearing capacity decrease rate in the shear wall at later loading stages.

The ultimate horizontal bearing capacities of the other four test pieces were all smaller than that of SRHCW-2 primarily due to the fact that the axial compression ratio of SRHCW-2 is higher. Horizontal bearing capacity decreased more slowly in SPRCW-7 and SPRCW-8 than SRHCW-2 upon reaching the peak. In other words, the embedded steel plates performed better in terms of delayed stiffness degeneration in the low-rise shear walls than concealed bracing and displayed better bearing capacity when the steel ratio was high.

3.4. Energy Dissipation Capacity of Test Pieces. Seismic performance in our test pieces was primarily dependent on the energy dissipation capacity of structural components when the structure entered the elastoplastic state under seismic action. Energy dissipation capacity is an important index reflective of the seismic performance of a given structure. The structural components convert energy to thermal energy for dissipation to the space mainly by means of plastic deformation. A plump hysteretic curve reflects favorable plastic deformation capacity in components. The area enveloped by the hysteretic loop is the energy dissipated by structural components. Here, we use the equivalent viscous damping coefficient h_e and the energy dissipation coefficient E to quantify the energy dissipation capacity of the test pieces. *Technical specification for seismic tests of buildings* (JGJ101-2015) [15] stipulates that E and h_e in each cycle be computed based on the area enveloped by the hysteretic loop in a hysteretic curve. The technique we used to compute this is illustrated in the diagram below.

Figure 13 shows the hysteretic curve for low-cycle repeated loading, where E and h_e are calculated as follows:

$$E = \frac{S_{(ABCD)}}{S_{(OEB)} + S_{(OFD)}}, \qquad h_e = \frac{E}{2\pi}. \tag{1}$$

Table 5 shows the energy dissipation coefficient, equivalent viscous damping coefficient h_e, and accumulated energy dissipation of SPRCW-5-8. The energy dissipation was negligibly small when the displacement was 0.9 mm.

A diagram for parallel comparison of accumulated energy dissipation between the four test pieces and SRHCW-2 is provided below.

Table 5 and Figure 14 altogether show the following findings:

(1) Greater loading displacement leads to greater energy dissipated in each cycle. The energy dissipation corresponding to the displacement before test piece failure accounts for about one-third of the accumulated energy dissipation.

(2) Accumulated energy dissipation of the test pieces, in order: SPRCW-8 > SPRCW-7 > SPRCW-5 > SPRCW-6. The accumulated energy dissipation of SPRCW-7 and SRRCW-8 was much higher than that of SPRCW-5 and SPRCW-6, which again indicates that steel plate ratio can significantly improve the energy dissipation capacity of low-rise shear walls of steel plate concrete. There are no significant rules with respect to the effects of the center-to-center distance of steel plates on such walls.

(3) Of the four test pieces, only SPRCW-8 showed larger accumulated energy dissipation than SRHCW-2. The embedded steel plates can more significantly increase the accumulated energy dissipation of low-rise shear walls than concealed bracing in the case of a high steel plate ratio and small steel plate spacing, and vice versa.

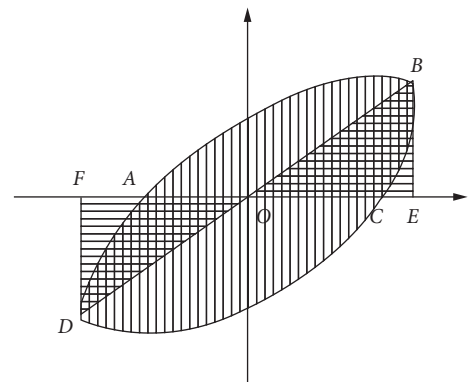

Figure 13: Equivalent viscous damping coefficient calculation.

Our comparative analysis of the equivalent viscous damping coefficients h_e of the four test pieces and SRHCW-2 is shown below.

Figure 15 shows the following findings:

(1) The equivalent viscous damping coefficients of SPRCW-5-SPRCW-8 increased as loading displacement increased. A larger loading displacement caused a higher percentage of plastic deformation in the test pieces, a plumper hysteretic curve, a larger area enveloped by the hysteretic loop, and greater dissipated energy. To this effect, the equivalent viscous damping coefficient also gradually increased with the displacement.

(2) The equivalent viscous damping coefficients of SPRCW-7 and SPRCW-8 increased at a slower rate than SPRCW-5 or SPRCW-6 in the later stages of loading, indicating that the percentages of plastic deformation in SPRCW-5 and SPRCW-6 rapidly increased to the point of failure late in the loading process. The equivalent viscous damping coefficients of SPRCW-7 and SPRCW-8, which had high steel ratio in the plates, increased relatively slowly in later stages of loading; their displacement loaded before failure was also larger than that of SPRCW-5 or SPRCW-6, indicating that increasing the steel plate ratio in the shear walls guarantees a stable increase in plastic deformation, larger ultimate displacement, and greater displacement of seismic energy in the shear wall.

(3) The equivalent viscous damping coefficients corresponding to the loading displacements of the four test pieces at two levels before failure are all significantly greater than the equivalent viscous

Table 5: Energy dissipation capacity of test pieces.

Test piece number	Cycle (mm)	Energy dissipation (kN·mm)	E	h_e (%)	Accumulated energy dissipation	Relative value
SPRCW-5	1.5	349.92	0.652	10.4	11272.18	1.000
	2.1	471.16	0.549	8.7		
	3.0	741.06	0.610	9.7		
	4.0	1109.49	0.584	9.3		
	5.0	1622.02	0.655	10.4		
	6.6	3020.37	0.941	15.0		
	8.0	3958.16	1.56	24.8		
SPRCW-6	1.5	365.60	0.648	10.3	10581.71	0.939
	2.1	521.73	0.578	9.2		
	3.0	857.42	0.632	10.1		
	4.0	1077.7	0.587	9.3		
	5.0	1706.94	0.747	11.9		
	6.6	2564.09	0.851	13.5		
	8.0	3488.23	1.239	19.7		
SPRCW-7	1.5	341.44	0.585	9.3	14611.01	1.296
	2.1	441.28	0.480	7.6		
	3.0	914.62	0.678	10.8		
	4.0	1418.57	0.760	12.1		
	5.0	1694.98	0.766	12.2		
	6.6	2392.25	0.773	12.3		
	8.0	3291.15	0.928	14.8		
	10	4116.72	0.978	15.6		
SPRCW-8	1.5	352.85	0.619	9.8	15612.89	1.385
	2.1	519.34	0.566	9.0		
	3.0	704.66	0.491	7.8		
	4.0	1236.23	0.638	10.2		
	5.0	1725.83	0.741	11.8		
	6.6	2750.19	0.889	14.1		
	8.0	3286.72	0.934	14.9		
	10.0	5037.07	1.301	20.7		

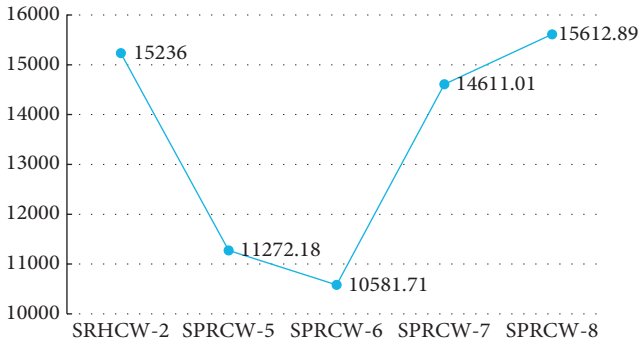

Figure 14: Comparison of accumulated energy dissipation.

damping coefficients corresponding to the previous loading displacements, indicating that the energy dissipation capacities of the test pieces reached the peak before failure during the loading process.

(4) The equivalent viscous damping coefficients of SPRCW-5 and SPRCW-6 were smaller than that of SRHCW-2 when displacement was smaller than 6.6 mm. The equivalent viscous damping coefficients of SPRCW-5 and SPRCW-6 were larger than that of SRHCW-2 when displacement exceeded 6.6 mm. The energy dissipation capacity of the low-rise shear

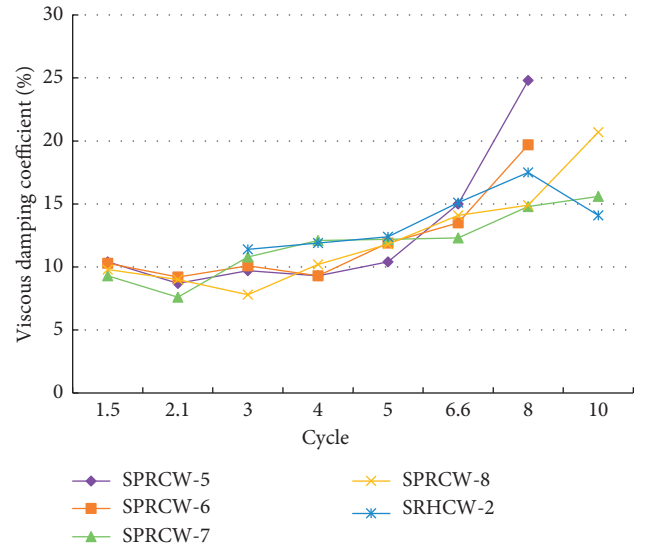

Figure 15: Comparison of equivalent viscous damping coefficients.

walls with smaller steel ratios was lower than that of the walls with concealed bracing when the displacement was small, and vice versa. The equivalent viscous damping coefficients of SPRCW-7 and SPRCW-8 are coincident with that of SRHCW-2.

There were minor differences in energy dissipation capacity between walls with high steel ratios and those with concealed bracing.

3.5. Intensity Attenuation in Test Pieces. Intensity attenuation is a process wherein the horizontal bearing capacity decreases as a number of loading cycles progresses due to the internal damage to a structural component during displacement loading. The intensity attenuation coefficient is typically used to measure the deformation resistance capacity of structural components. Here, the intensity attenuation coefficient β is the ratio of the horizontal bearing capacity in the second cycle of displacement loading at a certain level to the horizontal bearing capacity in the first cycle:

$$\beta = \frac{P_2}{P_1}. \quad (2)$$

Table 6 and Figure 16 show the following findings:

(1) There are minor differences in intensity attenuation coefficient among the four test pieces during loading until the final loading stage. There are also slight differences in intensity attenuation coefficient in each test piece under loads at different levels. The steel plate ratio and steel plate spacing have little effect on the intensity attenuation of low-rise shear walls before reaching the ultimate displacement.

(2) The intensity attenuation coefficient of SPRCW-5 corresponding to the loading displacement at the final level decreased only slightly. The intensity attenuation coefficient of SPRCW-7 corresponding to the loading displacement at the final level did not decrease but instead remained basically consistent during the whole loading process. On the contrary, the intensity attenuation coefficients of SPRCW-6 and SPRCW-8 corresponding to the loading displacement at the final level decreased substantially. It is thus clear that increasing the steel plate spacing decreases the degree of intensity attenuation in the low-rise shear wall and prevents any sudden intensity attenuation before failure.

4. Comparison of the Calculated Value of the Bearing Capacity of the Specimen and the Measured Value

The shear bearing capacity of the inclined section of the steel plate concrete shear wall under eccentric compression is checked by the formula 14.4.13 of the *Technical specification for concrete structure of high rise building* (JGJ3-2010) [17], and Table 7 is the comparison of the measured value and the calculated value of the shear bearing capacity of the specimen. It can be seen from Table 7 that the error between the calculated values of the horizontal bearing capacity of SPRCW-5 and SPRCW-6 and the measured values is very small, while the error of the calculated values of the horizontal bearing capacity of SPRCW-7 and SPRCW-8 and the measured values is very large. It can be seen that the formula for calculating the bearing capacity of the inclined section of the steel plate concrete shear wall under eccentric compression is suitable for the low steel plate with low steel plate and cold bending steel concrete low shear wall. For the high steel plate cold-formed steel reinforced concrete low-rise shear walls with high steel plate ratio, the formula should be improved and calculated.

Table 6: Intensity attenuation coefficient of test pieces.

Displacement (mm)	SPRCW-5	SPRCW-6	SPRCW-7	SPRCW-8
−10.0			0.93	0.76
−8.0		0.61	0.93	0.93
−6.6	0.88	0.92	0.95	0.94
−5.0	0.88	0.95	0.94	0.93
−4.0	0.95	0.98	0.85	0.94
−3.0	0.89	0.90	0.96	0.95
−2.1	0.98	0.95	0.96	0.91
−1.5	0.92	0.97	0.94	0.92
−0.9	0.95	0.91	0.98	0.85
0.9	0.93	0.85	0.88	0.93
1.5	0.93	0.95	0.95	0.92
2.1	0.92	0.93	0.89	0.99
3.0	0.85	0.95	0.91	0.94
4.0	0.86	0.92	0.93	0.92
5.0	0.92	0.93	0.93	0.97
6.6	0.82	0.88	0.94	0.88
8.0		0.8	0.91	0.91
10.0			0.92	0.73

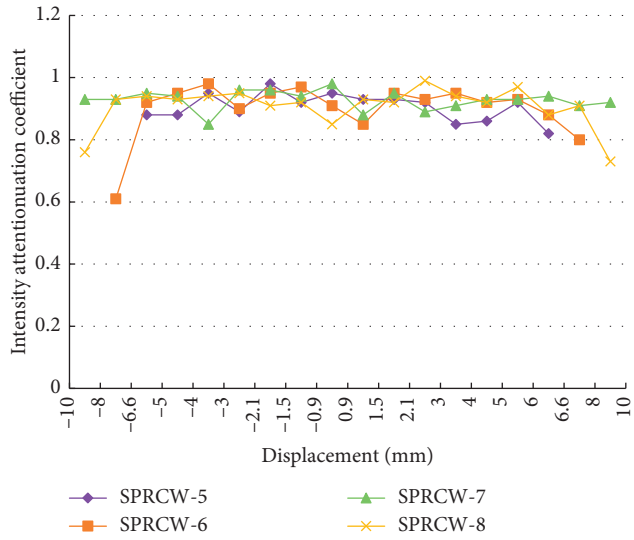

Figure 16: Intensity attenuation curve of test pieces.

Table 7: The shear bearing capacity comparison of specimens.

Test piece number	SPRCW-5	SPRCW-6	SPRCW-7	SPRCW-8
Measured value of horizontal bearing capacity (kN)	493.23	463.68	465.16	494.21
Calculated value (kN)	524.29	527.80	600.11	598.81
Calculation error (%)	6.30	13.83	29.01	21.16

5. Conclusion

We assessed the failure modes, hysteretic curves, skeleton curves, energy dissipation capacities, intensity attenuation, and other notable properties of four shear wall test pieces to reach the following conclusions.

(1) Embedded steel plates can effectively limit the widening and extension of wall cracks, increase the steel plate ratio, and thus improve the failure mode of the steel plate concrete low-rise shear wall while minimizing brittle failure.

(2) SPRCW-5-8 showed arch-shaped hysteretic curves with rheostriction effects less significant than SRHCW-2, indicating that no severe binding-slippage occurred between the steel plate and concrete after the four test pieces cracked in the test. The shearing studs welded onto both surfaces of the steel plate effectively limited the binding-slippage between the steel plate and concrete and guaranteed effective energy dissipation performance in the low-rise shear wall. We also found that the embedding of steel plates enhances the plastic deformation of the wall and absorbs seismic energy better than concealed bracing. Under the same conditions, increasing the steel spacing of the steel plate concrete shear walls effectively decelerates the decrease in horizontal bearing capacity of the shear wall upon reaching the ultimate load.

(3) The ultimate horizontal bearing capacities of the other four test pieces were all smaller than that of SRHCW-2 primarily due to the fact that the axial compression ratio of SRHCW-2 was higher. The horizontal bearing capacities of SPRCW-7 and SPRCW-8 decreased at a slower rate than SRHCW-2 when reaching the peak. The embedded steel plates performed better in terms of delaying stiffness degeneration in low-rise shear walls than concealed bracing and guaranteed effective bearing capacity in late loading stages when the steel plates had a high steel ratio.

(4) Increasing the steel plate spacing decreased the extent of intensity attenuation in low-rise shear walls and prevents any sudden attenuation in the walls before failure.

Data Availability

The data used to support the findings of this study are available from the corresponding author upon request

Conflicts of Interest

The authors declare that they have no conflicts of interest.

Acknowledgments

This study was supported by the National Natural Science Foundation of China (Grant no. 41372356). The authors gratefully acknowledge this support.

References

[1] R. G. Driver, G. L. Kulak, D. J. L. Kennedy, and A. E. Elwi, "Cyclic test of four-story steel plate shear wall," *Journal of Structure Engineering*, vol. 124, no. 2, pp. 112–120, 1998.

[2] X. D. Tong, J. F. Haijjar, and A. E. Schultz, "Cyclic behavior of steel frame structures with composite reinforced concrete infill walls and partially restrained connections," *Journey of Constructional Steel Research*, vol. 61, no. 4, pp. 531–552, 2005.

[3] A. Abrazadeh, M. Soltani, and A. Ayazi, "Experimental investigation of composite shear walls under shear loadings," *Thin-Walled Stuructures*, vol. 49, no. 7, pp. 842–854, 2011.

[4] J. H. Mun, K. H. Yang, and J. K. Song, "Shear behavior of squat heavyweight concrete walls with construction joints," *ACI Structural Journal*, vol. 114, no. 4, pp. 1019–1029, 2017.

[5] A. K. Marsono and S. Hatami, "Analysis of reinforced concrete shear walls with single band of octagonal openings," *KSCE Journal of Civil Eengineering*, vol. 20, no. 5, pp. 1887–1894, 2016.

[6] M. Y. Chen, R. Flkri, and C. C. Chen, "Experimental study of reinforced concrete and hybrid coupled shear wall systems," *Engineering Structures*, vol. 82, pp. 214–225, 2015.

[7] S. Mohebbi, S. R. Mirghaderi, F. Farahbod, A. B. Sabbagh, and S. Torabian, "Experimental on seismic behaviour of steel sheathed cold-formed steel shear walls cladded by gypsum and fiber cement boards," *Thin-Walled Structures*, vol. 104, pp. 228–247, 2016.

[8] Y. Y. Peng, J. R. Qian, and Y. H. Wang, "Cyclic performance of precast concrete shear walls with a mortar-sleeve connection for longitudinal steel bars," *Materials and Structures*, vol. 49, no. 6, pp. 2455–2469, 2016.

[9] M. S. Gorji and J. J. R. Cheng, "Plastic analysis and performance-based design of coupled steel plate shear walls," *Engineering Structure*, vol. 166, pp. 472–484, 2018.

[10] H. W. Tian, Y. Q. Li, and Y. Zhou, "Theoretical analysis and testing of steel frame with cold-formed steel shear walls with steel sheathing," *Journal of Structural Engineering*, vol. 144, no. 7, article 04018079, 2018.

[11] C. H. Zhai, B. Lu, W. P. Wen, D. F. Ji, and L. L. Xie, "Experimental study on shear behavior of tie-bars in steel-plate concrete composite structure subjected to cyclic loading," *Engineering Structures*, vol. 163, pp. 311–322, 2018.

[12] R. Aghayari and S. Dardaei, "Evaluating the effect of the thickness and yield point of steel on the response modification factor of RC frames braced with steel plate," *KSCE Journal of Civil Engineering*, vol. 22, no. 5, pp. 1865–1871, 2018.

[13] M. A. Dar, M. Yusuf, A. R. Dar, and J. Raju, "Experimental study on innovative sections for cold formed steel beams," *Steel and Composite Structures*, vol. 19, no. 6, pp. 1599–1610, 2015.

[14] S. Borzoo, S. R. M. Ghaderi, S. Mohebi, and A. Rahimzadeh, "Nonlinear finite element modeling of steel-sheathed cold-formed steel shear walls," *Steel and Composite Structures*, vol. 22, no. 1, pp. 79–89, 2016.

[15] JGJ 101-2015, *Technical Specification for Seismic Tests of Buildings*, China Standard Press, Beijing, China, 2015.

[16] GB/T 228-2010, *Technical Specification for Test of Metal Materials at Room Temperature*, China Standard Press, Beijing, China, 2010.

[17] JGJ3-2010, *Technical Specification for Concrete Structure of High Rise Building*, China Standard Press, Beijing, China, 2010.